Quantum Rate Constants from Short-Time Dynamics: An Analytic Continuation Approach†

Eunji Sim, Goran Krilov, and B. J. Berne*

Department of Chemistry, Columbia University, 3000 Broadway, New York, New York 10027

Received: November 28, 2000; In Final Form: January 19, 2001

A method for calculating the quantum canonical rate constant of chemical reactions in a many body system by means of a short-time flux autocorrelation function combined with a maximum entropy numerical analytic continuation scheme is presented. The rate constant is expressed as the time integral of the real-time flux autocorrelation function. The real-time flux autocorrelation function is evaluated for short times fully quantum mechanically by path integral Monte Carlo simulations. The maximum entropy approach is then used to extract the rate from the short real-time flux autocorrelation data. We present two numerical tests, one for proton transfer in harmonic dissipative environments in the deep tunneling regime and the other for the two-level model of primary charge separation in the photosynthetic reaction center. The results obtained using the flux autocorrelation data up to the time of no more than $\beta\hbar$ are in excellent agreement with the exact quantum calculation over a wide range of parameters including even the tunneling regime.

I. Introduction

The classical transition state theory (TST) is based on three assumptions: the electronic adiabaticity of the reaction, the adequacy of classical mechanics to describe the motion of the nuclei, and the fundamental (dynamical) assumption of no barrier recrossings. The latter implies that a reactive trajectory originating on the reactant side must cross the dividing surface only once and proceed to products. With these assumptions, classical TST gives an upper bound on the rate constant. Although classical TST is often accurate at sufficiently low temperatures, the correction factor for TST rates due to recrossing, known as the transmission coefficient, becomes smaller with increasing temperature because of the breakdown of the third assumption, i.e., more recrossings at high temperature.

Inspired by the success of classical TST, there have been numerous attempts to develop a quantum TST. These include the instanton model of a periodic orbit in pure imaginary time,[1] a semiclassical TST involving the conserved classical action variables at the transition state,[2] path integral centroid density approaches,[3−5] and various semiclassical models for including the effects of reaction path curvature on transition state tunneling probabilities.[6−9] Nevertheless, a uniquely well-defined quantum version of TST is still lacking. The reason for this is that the accurate treatment of tunneling through the dividing surface requires the solution of the quantum dynamics for motion near the transition state thus making it necessary to perform a full quantum dynamics simulation. Several comprehensive reviews of theoretical studies of quantum rate processes are available elsewhere.[10−12]

The formulation of the chemical reaction rate constant as a time integral of the flux autocorrelation function[13−17] is one of the most widely used theoretical models for predicting the rate constant of bimolecular chemical reactions in condensed phase systems. Practical application of this scheme, however, leads to an exponential increase in computational complexity with the number of participating degrees of freedom. The Feynman path integral approach[18−20] has been successfully used in computing equilibrium properties because the evaluation of multidimensional integrals in imaginary time can make use of stochastic importance sampling techniques.[21−24] However, extension of these methods to real time is still difficult because of the oscillatory nature of the real-time propagator which leads to dramatic phase cancellation and failure of MC schemes, known as the “sign problem”. In recent years, efforts to develop numerical techniques for evaluating path integrals in real time have been expanded significantly.[25−38] Early approaches to real-time path integrals were based on analytic continuation ideas,[25] brute-force stochastic integration of the real-time propagator,[26] coordinate rotation,[27,28] or stationary phase based MC methods,[29−31] in order to alleviate the sign problem.

Topaler and Makri introduced the quasiadiabatic propagator path integral (QUAPI) scheme[10,39] based on constructing a numerically exact quantum mechanical real-time path integral scheme for calculating correlation functions. The modified path integral expression involves one-dimensional propagators which describe the exact dynamics of the system along the adiabatic path, as well as a nonlocal influence functional that incorporates the multidimensional nonadiabatic corrections.[33] The QUAPI scheme allows the use of large time steps, resulting in the path integral dimensionality that is fairly small even for moderately long times. Although this method allows efficient sampling for short times, the statistical error nonetheless grows rapidly with the dimensionality of the integral.[34] Hence, other approximate methods for evaluating quantum correlation functions are needed.[40−44]

Rabani et al.[45] recently presented the reactive flux analytic continuation method, based on the quantum reactive flux formalism combined with a numerical analytic continuation approach to calculate quantum canonical rates in condensed phase systems with an explicit bath. They expressed the imaginary-time reactive flux correlation function in terms of a

---

† Part of the special issue “William H. Miller Festschrift”.

* To whom correspondence should be addressed.

10.1021/jp004307w CCC: $20.00

frequency dependent rate constant. The imaginary-time data was obtained by path integral Monte Carlo (PIMC) simulation and then analytically continued to real time using the maximum entropy (ME) method to obtain the reaction rate. A similar approach, using a numerical analytic continuation method, was studied by Plimak and Pollak,[46] who used a short-time inverse Laplace transform inversion technique. These approaches based on the combination of the path integral formalism and numerical analytic continuation methods[45,46] give reasonably accurate rate constants while using only imaginary-time data for the quantum rate calculations.

We have recently shown that the real-time correlation functions for finite temperature many body quantum systems can be easily obtained from analytic continuation of the short-time (in most cases up to $\beta\hbar$) symmetrized correlation function.[47] The short symmetrized real-time and the imaginary-time symmetrized correlation functions were evaluated directly using the PIMC technique and this was followed by a ME numerical analytic continuation to obtain the real-time correlation function. The computed real-time correlation functions were found to be in good agreement with exact results over several multiples of $\beta\hbar$ in time and exhibited a significant improvement over ME analytic continuation using only imaginary-time correlation data.[47] The quality of the inverted real-time correlation function considerably depends on the stability of the inversion kernel in the numerical analytic continuation process. The inversion kernel of the imaginary-time correlation data decays exponentially leading to highly unstable operation, whereas that of the symmetrized correlation data provides for more stable inversion. It was also found that the quantum coherences of a complex condensed phase system dissipate rather rapidly and the accurate quantum dynamics for times of order $\beta\hbar$ is sufficient to describe quantum effects in barrier crossing dynamics.[11] Thus, the use of an analytic continuation scheme to compute the power spectrum of a quantum time correlation function over the entire frequency range from the short-time dynamic data obtained using PIMC indeed seems to be a plausible alternative to solving the full quantum dynamics problem for various systems.

In this paper, we present the short-time analytic continuation by entropy maximization (STACEM) method for calculating the quantum canonical rate constant from the flux autocorrelation functions evaluated by path integral simulation for times considerably shorter than the plateau time. Starting with the flux correlation function formalism of Miller,[1] we derive working relations for the path integral expression for the flux autocorrelation function for the case of a system coupled to a bath described by a continuous spectral density. If the path integral ie expressed in terms of the discrete variable representation (DVR),[48−50] the propagator can be represented in a configurational space of significantly reduced dimensionality. It is possible to choose a DVR basis which allows the system propagator to be calculated exactly.[51] Employing a combination of such system-specific DVR quadratures and MC methods, we were able to obtain fairly accurate quantum results for thermally averaged rate constants under the various conditions relevant in chemical reactions, i.e., the crossover and deep tunneling regimes. We compare the rate constant obtained using the STACEM method with the “exact” results of QUAPI.[10] In section II, a brief description of the quantum canonical rate formulation is presented. The details of the path integral formalism for calculation of the flux autocorrelation function and the ME approach are discussed in sections III and IV, respectively. We present the results for two test systems including proton transfer and charge separation of the photosynthetic bacterial reaction center in section V, followed by the concluding remarks in section VI.

II. Rate Formulation

According to Miller et al.,[13] the Boltzmann averaged quantum mechanical canonical rate constant is given by

$$k = \frac{Z}{Z_r}\int_0^\infty dt\, C_F(t) \qquad (1)$$

where $C_F(t)$ is a flux autocorrelation function

$$C_F(t) = \frac{1}{Z}\mathrm{Tr}[\hat{F}\, e^{-\lambda H}\, e^{i\hat{H}t/\hbar}\, \hat{F}\, e^{-i\hat{H}t/\hbar}\, e^{-(\beta-\lambda)H}] \qquad (2)$$

The rate constant expression in eq 1 is valid for any value of λ from 0 to β. In this study, we chose the value of $\lambda = \beta/2$. This choice of λ leads to a symmmetric form of the flux autocorrelation function involving forward and backward complex time propagators analogous to the symmetrized correlation function introduced by Berne and co-workers[52,53]

$$G_F(t) = \frac{1}{Z}\mathrm{Tr}[\hat{F}\, e^{i\hat{H}t_c^*/\hbar}\, \hat{F}\, e^{-i\hat{H}t_c/\hbar}] \qquad (3)$$

Here $\hat{F}$ is the symmetrized flux operator

$$\hat{F} = \frac{1}{2m_s}[\hat{p}_s\, \delta(\hat{s}) + \delta(\hat{s})\, \hat{p}_s] \qquad (4)$$

and, for the sake of simplicity, the dividing surface through which the reactive flux is measured is located at $s = 0$. Finally, $t_c = t - i\beta\hbar/2$ is a complex time that arises from combining the time evolution operator with the Boltzmann operator and $\beta = 1/k_BT$. Z and Z_r denote the total canonical partition function and the reactant side partition function, respectively, such that

$$\frac{Z}{Z_r} = \frac{\mathrm{Tr}[e^{-\beta E}]}{\mathrm{Tr}[e^{-\beta E}\hat{h}_r]} \qquad (5)$$

with $\hat{h}_r$ being the reactant side projection operator. Because the correlation function is an even function of time, one can change the integration range and the rate is given by

$$k = \frac{1}{2}\int_{-\infty}^{\infty} dt\, G'_F(t) \qquad (6)$$

where $G'_F(t)$ includes the partition function ratio prefactor. One can then define a frequency dependent rate constant $k(\omega)$:

$$k(\omega) = \frac{1}{2}\int_{-\infty}^{\infty} dt\, e^{i\omega t} G'_F(t) \qquad (7)$$

such that the zero frequency value of $k(\omega)$ corresponds to the rate in eq 6. To relate the frequency dependent rate to the short-time flux autocorrelation data, we invert eq 8:

$$G'_F(t) = \frac{1}{\pi}\int_{-\infty}^{\infty} d\omega\, e^{-i\omega t} k(\omega) \qquad (8)$$

Typically, in practice, the integration range in eq 1 extends to the conventional plateau time. Although various numerical techniques provide accurate short-time quantum correlation functions, evaluating a quantum correlation function for long times (i.e., the order of plateau time) is not possible for most condensed phase systems. However, by inverting eq 8, one can calculate the frequency dependent rate constant from short-time correlation function data. Therefore, estimating $k(\omega)$ by analytic continuation of short-time $G'_F(t)$ data to $t = \infty$ presents a practical alternative means of rate calculation. The details of path integral representation of the symmetrized flux autocorrelation function and the inversion technique used in this study will be discussed in the following sections.

III. Path Integral Formulation of Flux Autocorrelation Function

Consider a one-dimensional quantum mechanical system interacting with a thermal bath, which is represented by Q-harmonic oscillators. The bath modes do not interact with each other directly but only through the interaction with the system such that

$$H = H_s(s) + H_b(\vec{x}) + V_I(s,\vec{x}) \tag{9}$$

where the interaction between the system and bath has linear form

$$V_I(s,\vec{x}) = -s\sum_{n=1}^{Q} c_n x_n \tag{10}$$

with s being the system coordinate and $\vec{x} = \{x_n, n = 1, ..., Q\}$ the bath coordinates.

For the case of the Hamiltonian in eq 9, evaluating the trace in eq 3 including the partition function ratio gives

$$G'_F(t) = \frac{\hbar^2}{4Z_r m_s^{\,2}\,\Delta_s^{\,2}}[K(\Delta_s,\Delta_s,0,0;t_c) - K(0,\Delta_s,0,\Delta_s;t_c) + K(0,0,\Delta_s,\Delta_s;t_c) - K(\Delta_s,0,\Delta_s,0;t_c)] \tag{11}$$

where Δ_s arises from the finite difference derivatives, such that, Δ_s is a coordinate point sufficiently close to the dividing surface. Note that the right-hand side of the equation can be further simplified to twice the real part of the first two propagators. However, using four propagator terms as shown above makes the sampling function smoother which improves the efficiency of MC simulation.

The path integral expression for the propagator in eq 11 is given by

$$\begin{aligned} K(s_0,s_N,s_{N+1},s_{2N+1};t_c) &\equiv \int_{-\infty}^{\infty} \mathrm{d}^Q\vec{x}_0\, \langle \vec{x}_0|\langle s_{2N+1}|\mathrm{e}^{-iHt_c^*/\hbar}|s_{N+1}\rangle \langle s_N|\mathrm{e}^{-iHt_c/\hbar}|s_0\rangle\vec{x}_0\rangle \\ &= \int_{-\infty}^{\infty}\mathrm{d}s_1 \cdots \int_{-\infty}^{\infty}\mathrm{d}s_{N-1}\int_{-\infty}^{\infty}\mathrm{d}s_{N+2} \cdots \int_{-\infty}^{\infty}\mathrm{d}s_{2N} \prod_{k=N+1}^{2N+1}\langle s_k|\mathrm{e}^{iH_s\Delta t_c^*/\hbar}|s_{k-1}\rangle \\ &\quad \prod_{k=1}^{N}\langle s_k|\mathrm{e}^{-iH_s\Delta t_c/\hbar}|s_{k-1}\rangle I(s_0,...,s_{2N+1};\Delta t_c) \end{aligned} \tag{12}$$

which results from symmetric Trotter splitting of the total Hamiltonian[10] into a system dependent part and a bath part including the system−bath interaction such that

$$\langle s\vec{x}|\exp(-iH\Delta t_c/\hbar|s'\vec{x}'\rangle = \int_{-\infty}^{\infty}\mathrm{d}^Q\vec{x}''\,\langle\vec{x}|\mathrm{e}^{-iH'_b(s)\Delta t_c/2\hbar}|\vec{x}''\rangle\langle s|\mathrm{e}^{-iH_s\Delta t_c/\hbar}|s'\rangle \langle\vec{x}''|\mathrm{e}^{-iH'_b(s')\Delta t_c/2\hbar}|\vec{x}'\rangle \tag{13}$$

where $\mathrm{H}'_b = H_b + V_I$. This type of splitting ensures that propagators are accurate over large time steps, $\Delta t_c = t_c/N$, so the total number of time slices and thus the dimension of the discretized path integral is relatively small. Implementation of QUAPI[33] allowed the use of even larger time steps with a counter-term corrected reference system potential. $I(s_0,...,s_{2N+1};\Delta t_c)$ is an influence functional that arises from the coupling to the environment. Because there is no direct interaction between bath modes, the influence functional produced by the environment can be written in product form:[54]

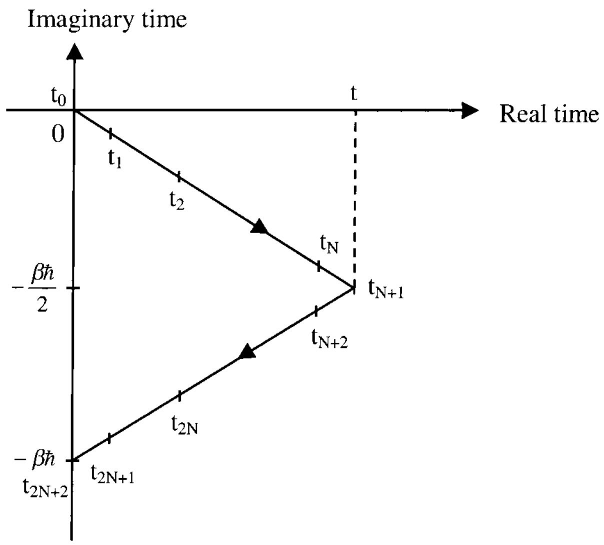

Figure 1. Schematic representation of the propagation contour appearing in the symmetrized time correlation function in the complex time plane. Discretized time points resulting from the symmetrized splitting of the propagator (see text) are denoted. Note the half time step near end points. The arrows indicate the direction of propagation.

$$I(s_0,...,s_{2N+1};\Delta t_c) = \prod_{n=1}^{Q} I_n(s_0,...,s_{2N+1};\Delta t_c) \tag{14}$$

where

$$\begin{aligned} I_n(s_0,...,s_{2N+1};\Delta t_c) = \int_{-\infty}^{\infty}\mathrm{d}x_{n,0}\,\langle x_{n,0}|\mathrm{e}^{iH'_{b,n}(s_{2N+1})\Delta t_c^*/2\hbar} \\ \mathrm{e}^{iH'_{b,n}(s_{2N})\Delta t_c^*/\hbar} \cdots \mathrm{e}^{iH'_{b,n}(s_{N+2})\Delta t_c^*/\hbar}\,\mathrm{e}^{iH'_{b,n}(s_{N+1})\Delta t_c^*/2\hbar} \times \\ \mathrm{e}^{iH'_{b,n}(s_N)\Delta t_c/2\hbar}\,\mathrm{e}^{-iH'_{b,n}(s_{N-1})\Delta t_c/\hbar} \cdots \mathrm{e}^{-iH'_{b,n}(s_1)\Delta t_c/\hbar} \times \\ \mathrm{e}^{-iH'_{b,n}(s_0)\Delta t_c/2\hbar}|x_{n,0}\rangle \end{aligned} \tag{15}$$

where the Hamiltonian $H'_{b,n}(x_n;s)$ is a function of nth bath mode coordinate and the system coordinate. The closed form of the influence functional integral exists only for the very special case of a harmonic bath with linear coupling. For nonlinear couplings the integral in eq 15 cannot be computed exactly even with the harmonic bath. However, if the coupling is weak and the anharmonicity is not large, one may compute the influence functional perturbatively.[55]

The influence functional computed exactly for the case of the harmonic bath with bilinear coupling has the form

$$I = \exp\left\{-\frac{1}{\hbar}\int_\Gamma \mathrm{d}t_1 \int_\Gamma^{t_1} \mathrm{d}t_2\, \alpha(t_1,t_2)\, s(t_1)\, s(t_2)\right\} \tag{16}$$

where the subscript Γ indicates that the time integration is performed over the complex time contour shown in Figure 1. The bath response function for the interaction potential in eq 10 is

$$\alpha(t_1,t_2) = \frac{1}{\hbar}\sum_{n=1}^{Q} c_n^{\,2}\{\langle x_n(t_1)x_n(t_2)\rangle - \langle x_n\rangle^2\} = \sum_{n=1}^{Q} \frac{c_n^{\,2}\cos(\omega_n\Delta t + i\beta\omega_n\hbar/2)}{2m_n\omega_n\sinh(\beta\omega_n\hbar/2)} \tag{17}$$

where $\Delta t = t_b - t_a$ with t_b being the later time point than t_a in the direction of the contour. The averages are performed over the nth bare bath mode at inverse temperature β. In this paper, the characteristics of the bath are captured by the continuous spectral density

$$J(\omega) = \frac{\pi}{2}\sum_{n=1}^{Q}\frac{c_n^{\,2}}{m_n\omega_n}\,\delta(\omega-\omega_n) \tag{18}$$

To take advantage of compact representation of a smaller basis set size provided by the use of the DVR,[10,50] we discretize the path integral expression of the propagator in eq 12 as follows:

$$\begin{aligned} K(s_0,s_N,s_{N+1},s_{2N+1};t_\mathrm{c}) = {} & \sum_{k_0}^{M}\cdots\sum_{k_{2N+1}}^{M} \langle s_{2N+1}|u_{k_{2N+1}}\rangle\,\langle u_{k_{N+1}}|s_{N+1}\rangle \\ & \times \langle s_N|u_{k_N}\rangle\,\langle u_{k_0}|s_0\rangle \prod_{j=N+1}^{2N}\langle u_{k_{j+1}}|\mathrm{e}^{iH_\mathrm{s}\Delta t_\mathrm{c}^*/\hbar}|u_{k_j}\rangle \\ & \times \prod_{j=0}^{N-1}\langle u_{k_{j+1}}|\mathrm{e}^{-iH_\mathrm{s}\Delta t_\mathrm{c}/\hbar}|u_{k_j}\rangle\, I(\tilde{s}_{k_0},\ldots,\tilde{s}_{k_{2N+1}};\Delta t_\mathrm{c}) \end{aligned} \tag{19}$$

where $\{u_l\}$ and $\{\tilde{s}_l\}$ are the DVR eigenstates and eigenvalues, respectively, that are obtained by diagonalizing the position matrix of the M lowest energy eigenstates, $\{\Phi_l;\, E_l,\, l = 1, ..., M\}$. In addition to a tremendous reduction of configuration space, a system-specific DVR also has the benefit of allowing the exact calculation of the short-time system propagator in an exact manner as shown

$$\langle u|\mathrm{e}^{-iH_\mathrm{s}\Delta t_\mathrm{c}/\hbar}|u'\rangle = \sum_{l=1}^{M}\mathrm{e}^{-iE_l\Delta t_\mathrm{c}/\hbar}\langle u|\Phi_l\rangle\langle\Phi_l|u'\rangle \tag{20}$$

The transformation coefficients $\langle u|\Phi_l\rangle$ are obtained automatically during the construction of DVR states. The total number of integrals that need to be evaluated is equal to M^{2N+2}. It is thus essential that M be as small as possible.

In similar fashion, the influence functional can be rewritten in a discretized form as the following:

$$I(\tilde{s}_{k_0},\ldots,\tilde{s}_{k_{2N+1}};\Delta t_\mathrm{c}) = Z_b \exp\left\{-\frac{1}{\hbar}\sum_{j=0}^{2N+1}\sum_{j'=0}^{j} A_{k_jk_{j'}}\,\tilde{s}_{k_j}\,\tilde{s}_{k_{j'}}\right\} \tag{21}$$

where $\tilde{s}_{k_j} = \tilde{s}(t_j)$ along the contour shown in Figure 1, which is discretized as follows:

$$\begin{aligned} t_0 &= 0 \\ t_j &= (j - 1/2)(\Delta t - i\Delta\beta\hbar), \quad 1 \le j \le N \\ t_{N+1} &= t_\mathrm{c} = t - i\beta\hbar/2 \\ t_j &= \left(2N - \frac{2j-3}{2}\right)(\Delta t + i\Delta\beta\hbar) - i\beta\hbar, \\ & \qquad N+2 \le j \le 2N+1 \\ t_{2N+2} &= -i\beta\hbar \end{aligned} \tag{22}$$

where $\Delta t = t/N$ and $\Delta\beta = \beta/2N$. The diagonal coefficients of the influence functional exponent are computed as follows:

$$A_{kk} = \frac{2}{\pi}\int_0^\infty \mathrm{d}\omega\,\frac{J(\omega)}{\omega^2\sinh(\hbar\omega\beta/2)}\sin[\omega(t_{k+1} - t_k + i\hbar\beta)/2]\,\sin[\omega(t_{k+1} - t_k)/2] \tag{23}$$

whereas the offdiagonal coefficients are given by

$$A_{kk'} = \frac{4}{\pi}\int_0^\infty \mathrm{d}\omega\,\frac{J(\omega)}{\omega^2\sinh(\hbar\omega\beta/2)} \cos[\omega(t_{k+1} + t_k - t_{k'+1} - t_{k'} + i\hbar\beta)/2]\,\sin[\omega(t_{k+1} - t_k)/2]\,\sin[\omega(t_{k'+1} - t_{k'})/2], \qquad k \neq k' \tag{24}$$

Even though in some cases full discretized space integration is possible, most problems still require stochastic sampling. The discretized representation of the flux autocorrelation function involves $2N + 2$ integrations. The Boltzmann factors in eq 3 lead to damped propagators, so that the integrand has significant amplitude only in certain localized regions of this $(2N+2)$ dimensional space. This property allows the use of MC sampling methods to evaluate the quantum correlation functions. Still the convergence of such schemes depends critically on the smoothness of the integrand as well as on the dimensionality of the integral.

For simplicity, we rewrite the discretized symmetrized flux autocorrelation function path integral expression as

$$G_\mathrm{F}'(t) = \frac{\hbar^2}{4Z_\mathrm{r}m_\mathrm{s}^{\,2}\,\Delta_\mathrm{s}^{\,2}}\sum_{k_0}^{M}\cdots\sum_{k_{2N+1}}^{M} A(k_0,k_N,k_{N+1},k_{2N+1})\,P(k_0,\ldots,k_{2N+1};\Delta t_\mathrm{c}) \tag{25}$$

The operator A includes the end-point projection operators of four propagators in eq 11 and is given by

$$\begin{aligned} A(k_0,k_N,k_{N+1},k_{2N+1}) = {} & \langle 0|u_{k_{2N+1}}\rangle\,\langle u_{k_{N+1}}|0\rangle\,\langle\Delta_\mathrm{s}|u_{k_N}\rangle\langle u_{k_0}|\Delta_\mathrm{s}\rangle \\ & - \langle\Delta_\mathrm{s}|u_{k_{2N+1}}\rangle\,\langle u_{k_{N+1}}|0\rangle\,\langle\Delta_\mathrm{s}|u_{k_N}\rangle\langle u_{k_0}|0\rangle \\ & + \langle\Delta_\mathrm{s}|u_{k_{2N+1}}\rangle\,\langle u_{k_{N+1}}|\Delta_\mathrm{s}\rangle\,\langle 0|u_{k_N}\rangle\langle u_{k_0}|0\rangle \\ & - \langle 0|u_{k_{2N+1}}\rangle\,\langle u_{k_{N+1}}|\Delta_\mathrm{s}\rangle\,\langle 0|u_{k_N}\rangle\langle u_{k_0}|\Delta_\mathrm{s}\rangle \end{aligned} \tag{26}$$

whereas $P(k_0, ..., k_{2N+1};\Delta t_\mathrm{c})$ includes the rest of system propagators as well as the influence functional. Using similar notation, the reactant partition function is

$$Z_\mathrm{r} = \sum_{k_0}^{M}\cdots\sum_{k_{2N+1}}^{M} B(k_0,k_N,k_{N+1},k_{2N+1})\,P(k_0,\ldots,k_{2N+1};\Delta t_\mathrm{c}) \tag{27}$$

with

$$B(k_0,k_N,k_{N+1},k_{2N+1}) = \delta_{k_0,k_{2N+1}}h_\mathrm{r}(k_N)\delta_{k_N,k_{N+1}} \tag{28}$$

where $\delta_{k,k'}$ represents Kronecker delta function and h_r is equal to 1 for $\tilde{s}_{k_N} < 0$ and is zero otherwise.

To compute the real-time flux autocorrelation function, we perform two separate open chain PIMC simulations on a $(2N + 2)$ dimensional DVR grid. The one-dimensional system propagator is calculated according to eq 20 and stored as a complex valued matrix on a DVR grid. The indices of the DVR states are incremented (or decremented) during each MC step by a randomly selected index spacing. For the purpose of simulation, we write the symmetrized flux autocorrelation function as

$$G'_{\mathrm{F}}(t) = \frac{\hbar^2}{4 Z_{\mathrm{r}} {m_{\mathrm{s}}}^2 \, {\Delta_{\mathrm{s}}}^2} \chi \zeta \tag{29}$$

The simulation consists of two stages. First, as specified in Thirumalai and Berne,[53] the sign of numerator χ is evaluated by using the absolute value of the real part of the numerator as the unnormalized sampling function:

$$\chi = \left\langle \frac{\mathrm{Re}[AP]}{\rho_1} \right\rangle_{\rho_1} \tag{30}$$

where

$$\rho_1(k_0,...,k_{2N+1};\Delta t_{\mathrm{c}}) = \left| \mathrm{Re}[A(k_0,...,k_{2N+1}) P(k_0,...,k_{2N+1};\Delta t_{\mathrm{c}})] \right| \tag{31}$$

In the second stage, the ratio ζ of the normalization integral divided by the reactant partition function is computed, and

$$\zeta = \frac{\langle \rho_1/\rho_2 \rangle_{\rho_2}}{\langle [BP]/\rho_2 \rangle_{\rho_2}} \tag{32}$$

where

$$\rho_2(k_0,...,k_{2N+1};\Delta t_{\mathrm{c}}) = \left| \mathrm{Re}[\Omega(k_N) P(k_0,...,k_{2N+1};\Delta t_{\mathrm{c}})] \right| \tag{33}$$

The artificial factor $\Omega(k_N)$ is introduced so that the effect of system operator A is included in the sampling function:

$$\Omega(k_N) = \begin{cases} \epsilon, \text{ if } \tilde{s}_{k_N} \text{ is near the dividing surface} \\ 1, \text{ if otherwise} \end{cases}$$

and ϵ is an adjustable constant parameter.

IV. Maximum Entropy Method

In the approach described above, the determination of the quantum canonical rate from short real-time data requires the inversion of the integral eq 8 to solve for the frequency dependent rate constant $k(\omega)$. The frequency zero mode value $k(0)$ then corresponds to the experimentally observable reaction rate. In this study, the flux autocorrelation function $G'_{\mathrm{F}}(t)$ is known only for a short-time interval (generally $t < \beta\hbar$), and therefore, the inversion of eq 8 represents a numerical analytic continuation of the flux autocorrelation function to $t = \infty$. Because the data obtained from simulations is incomplete and noisy, the analytic continuation of eq 8 is an ill-posed problem. In other words, there is an infinite number of $k(\omega)$ that satisfy eq 8 within statistical noise limits for a given set of short-time flux autocorrelation data. Hence, there is clearly a need for a way of selecting the "best solution" from the set of possible solutions.

Recently, Bayesian ideas have been used to deal with the ill-posed nature of analytically continuing the noisy imaginary-time MC data to real time. One of the most widely used approaches is the ME method.[56] The method requires only that the transformation which relates the data and the solution be known. Furthermore, ME allows the inclusion of prior knowledge about the solution in a logically consistent fashion. As such, the method is well-suited for solving ill-posed mathematical problems.

The methods of ME have been successfully applied in the context of analytic continuation for a variety of quantum systems such as various quantum lattice models,[57] the study of light absorption spectra,[47,58−60] and vibrational line shapes.[47,60−62] More recently, the method was successfully applied to analytic continuation of the imaginary-time flux autocorrelation functions.[45]

For the purpose of the ME approach, we rewrite the integral equation, eq 8, as

$$D(t) = \int \mathrm{d}\omega \, K(t,\omega) \, A(\omega) \tag{34}$$

In this notation, $D(t) \equiv G'_{\mathrm{F}}(t)$ is the data (in this case the short-time flux autocorrelation function), $K(t,\omega)$ is the Fourier kernel, and $A(\omega)$ is the solution, referred to as the map, corresponding to $k(\omega)$. ME principles provide a way to choose the most probable solution which is consistent with the data through the methods of Bayesian inference. Typically, the data is known only at a discrete set of points $\{t_j\}$, and we likewise seek the solution at a discrete set of points $\{\omega_k\}$. The ME method selects the solution which maximizes the posterior probability or the probability of the solution $\vec{A}$ given a data set $\vec{D}$. Using the Bayes theorem, one can show that[56,57] the posterior probability is given by

$$P(\vec{A}|\vec{D}) \propto \exp(\alpha S - \chi^2/2) = \mathrm{e}^{Q} \tag{35}$$

Here χ^2 is the standard mean squared deviation from the data

$$\chi^2 = \sum_{j,k} (D_j - \sum_l K_{jl} A_l)[C^{-1}]_{jk} (D_k - \sum_l K_{kl} A_l) \tag{36}$$

where C_{jk} is the covariance matrix

$$C_{jk} = \frac{1}{N_m(N_m - 1)} \sum_{l=1}^{N_m} (\langle D_j \rangle - D_j^{(l)})(\langle D_k \rangle - D_k^{(l)}) \tag{37}$$

with N_m being the number of measurements. In this study, the data points are calculated independently so the covariance matrix is diagonal, and therefore the expression for χ^2 reduces to

$$\chi^2 = \sum_j \frac{(D_j - \Sigma_l K_{jl} A_l)^2}{{\sigma_j}^2} \tag{38}$$

where σ_j are the standard deviations of each data point, i.e., the square root of the diagonal elements of the covariance matrix.

S is the information entropy, the form of which is axiomatically chosen to be

$$S = \sum_k \Delta\omega \left(A_k - m_k - A_k \ln \frac{A_k}{m_k} \right) \tag{39}$$

In this formulation, the entropy is measured relative to a default model $m(\omega)$ which can contain prior information about the solution and α is a positive regularization parameter.

Obtaining the ME solution then involves finding a map $\vec{A}$ which maximizes the posterior probability and is therefore a maximization problem in N_a variables, where N_a is the number of points $\{\omega_k\}$ at which the solution is evaluated. The solution obtained in this way is still conditional on the arbitrary parameter α, which can be interpreted as a regularization parameter controlling the smoothness of the map. Large values of α lead to a result primarily determined by the entropy function and, hence, the default model. Small values of α in turn lead to a map determined mostly by the χ^2 and thus to a closer fitting of the data. The principal drawback is that, along with the data, the errors would be fit as well.

In this study, α is selected according to the L-curve method.[63,64] In this context, we regard the entropy as the regularizing function parametrically dependent on α. The value of α is selected by constructing a plot of $\log[-S(\vec{A})]$ vs $\log \chi^2$. This curve has a characteristic L shape, and the corner of the L, or the point of maximum curvature, corresponds to the value of α which is the best compromise between fitting the data and obtaining a smooth solution. It should be noted that there are other possible ways of selecting the regularization parameter, such as a Bayesian approach of classic ME.[57,65] However, in general, we observed that provided the data is of sufficient quality, the inversion result is fairly insensitive to the particular choice of the regularization parameter, exhibiting only minor variations over several orders of magnitude of α. In addition, the L-curve method provides a way of qualitatively assessing the quality of the input data, with a sharper L curve signifying better quality data. The quality of the data in general depends on the accuracy of the data itself (the size of the error bars) as well as on how well the error bars themselves are estimated.

We employ a maximization algorithm due to Bryan,[66] which reduces the space in which the search for the solution is performed. The kernel is first factored using singular value decomposition $\mathbf{K} = \mathbf{V}\Sigma\mathbf{U}^{\mathrm{T}}$. Because the space spanned by the rows of $\mathbf{K}$ is the same as that spanned by the columns of $\mathbf{U}$ associated with nonsingular eigenvalues, the search for the solution can be performed in this singular space of dimensionality N_s, where N_s is the number of nonsingular eigenvalues. The solution in singular space is expressed in terms of the vector $\vec{u}$, which is related to the N_a dimensional map space via

$$A_j = m_j \exp\left(\sum_{l=1}^{N_s} U_{jl} u_l\right) \tag{40}$$

This exponential transformation is useful because it ensures the positivity of the solution.

Prior knowledge of the solution may be used to select a map $m(\omega)$ that resembles the true solution, which may improve the quality of the inversion. However, in doing this, there is a danger of introducing a bias which may significantly reduce the quality of the inversion in some cases, such as if the true solution differs appreciably from the expectation based on prior knowledge. Hence, care must be taken in selecting a specific model. To avoid this problem, in this study, we use a flat default map, which satisfies a known sum rule, such as the integral of $k(\omega)$ over ω, which does not bias the solution toward a particular feature. This model was found to be adequate for the purpose of this study. In addition, we found that the solution does not vary significantly with the number of input data points. In particular, doubling the number of data points at which $G_F'(t)$ is evaluated within a given time range leads to an inversion that differs very slightly (less than one percent) from that obtained using a smaller number of data points.

Because of the nature of the ME method it is not possible to assign error bars to values of the map at specific frequencies. Therefore, it was not possible to assign an error bar to the rate constant, which corresponds to a particular map point at $\omega = 0$. Instead, we estimate the accuracy through comparison with the exact results.

V. Numerical Examples

In this section, we present examples that illustrate the advantages of the STACEM method discussed in this paper, including proton transfer in condensed media and charge separation of the photosynthetic bacterial reaction center. In both cases, the bath is described by the spectral density with the Ohmic form

$$J(\omega) = \eta\omega \exp\left\{-\frac{\omega}{\omega_c}\right\} \tag{41}$$

A. Proton Transfer. We model a typical proton transfer reaction as a double well linearly coupled to a harmonic environment. This particular system was chosen to allow comparison of the results obtained by our method with those obtained from the exact quantum mechanical calculation.[10] The potential along the reaction coordinate s is a symmetric double well:

$$V_s = -\frac{1}{2}a_1 s^2 + \frac{1}{4}a_2 s^4 \tag{42}$$

with the potential parameters

$$a_1 = m_s\omega_b^{\ 2}, \quad a_2 = \frac{a_1^{\ 2}}{4E_b} \tag{43}$$

where m_s is the system mass, ω_b is the barrier frequency and E_b is the barrier height. This potential has minima at $s = \pm (a_1/a_2)^{1/2}$ and a barrier at $s = 0$. Corresponding potential parameters are the proton mass $m_s = 1836$ au, $\omega_b = 500$ cm^{-1}, and $E_b = 2085$ cm^{-1} (this is the same potential referred to as DW1 in ref 10). The bath is described by a spectral density of ohmic form given in eq 41 with the cutoff frequency of $\omega_c = 500$ cm^{-1}. The rate is studied as a function of the friction constant as well as the temperature.

The bath Hamiltonian which includes the renormalization term is given by

$$H_b = \sum_{n=1}^{Q} \left\{ \frac{1}{2} M_n \dot{x}_n^{\ 2} + \frac{1}{2} M_n \omega_n^{\ 2} \left(x_n - \frac{c_n s}{2M_n\omega_n^{\ 2}} \right)^2 \right\} \tag{44}$$

A physically relevant description of the problem should include another renormalization term in the system potential. In this study, however, we deliberately removed the extra renormalization potential in order to explore the dynamic effect of the friction strength without changing the barrier height of the reaction coordinate.

PIMC sampling is performed to calculate the short-time symmetrized flux autocorrelation function $G_F'(t)$ as discussed in section III. Depending on temperature and friction strength, we found that 5−12 DVR states and 5−7 time slices are sufficient to achieve the converged results. The MC trajectories consisted of 5×10^8−10^9 MC steps per time slice. At each MC step, a segment of path is selected randomly and the indices of DVR states corresponding to time slices of that path segment are shifted by a randomly chosen integer from $-m$ to m where $m < M$. Using the compact basis set of DVR states leads to error bars that are bounded rather than the unbounded exponential growth of statistical error that characterizes real-time MC simulations using a continuous coordinate representation.

Figure 2 shows typical reactive flux correlation functions computed by the ME method to illustrate the validity of using analytic continuation of short-time dynamic data for extracting

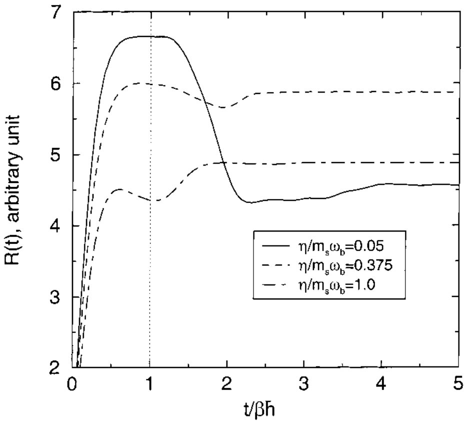

Figure 2. Analytically continued results of reactive flux correlation functions, eq 45, in arbitrary units as a function of time at $T = 200$ K. The friction strength, $\eta/m_s\omega_b$, of the solid line is 0.05, the dashed line 0.3752, and the dot−dashed line 1.0. Dotted line indicates the time up to which the symmetrized correlation function data was computed by simulation and analytically continued. Note the recrossing and crossing events predicted by ME method occur after the cutoff time $\beta\hbar$.

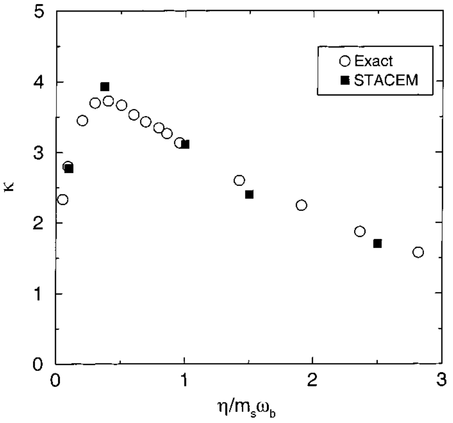

Figure 3. Quantum transmission coefficient of proton transfer as a function of the friction strength at $T = 200$ K. Hollow circles are the numerically exact results from Figure 9b of ref 10. The rates obtained by the method presented in this paper are shown by solid squares using path integral Monte Carlo data of the flux autocorrelation function up to $\beta\hbar = 1578$ au.

the long-time dynamics. The long-time behavior of the reactive flux correlation functions (to the right side of the vertical dotted line) is determined by analytically continuing the simulation data available up to $t = \beta\hbar$ (left side of the vertical dotted line). The reactive flux correlation function is a time integral of the symmetrized flux autocorrelation function

$$R(t) = \int_0^t \mathrm{d}t'\, G_F'(t') \tag{45}$$

For the purpose of comparison, the units of the reactive flux correlation functions in Figure 2 are arbitrarily scaled. Note that there are dynamically important events that occur after the time $t = \beta\hbar$ and all three friction strength cases well illustrate that the long-time behavior of crossing and recrossing events of reactive flux is successfully predicted by the analytic continuation procedure.

Figure 3 shows the transmission coefficient as a function of the static friction coefficient $\eta/m_s\omega_b$ in comparison with the results from the exact quantum calculation. The quantum transmission coefficient is the ratio of the true rate constant divided by the classical TST rate, i.e., $\kappa = k/k_{\mathrm{TST}}$, where k_{TST} is the classical TST rate given by

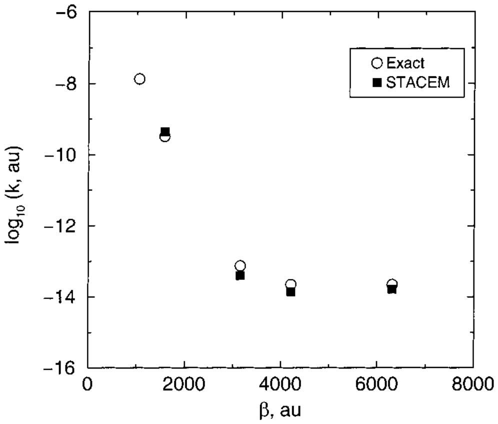

Figure 4. Logarithm of the rate constant as a function of inverse temperature for the friction strength, $\eta/m_s\omega_b = 0.05$. Hollow circles are the numerically exact results from Figure 12 of ref 10 and the rates obtained by the method presented in this paper are shown by solid squares. For each temperature point, the flux autocorrelation function is used up to $\beta\hbar = \hbar/k_BT$ au. Note the temperature independence of the rate in deep tunneling regime.

$$k_{\mathrm{TST}} = \frac{\omega_b}{\sqrt{2\pi}}\, \mathrm{e}^{-\beta E_b} \tag{46}$$

Our results are in excellent agreement with the QUAPI numerical results[10] over the entire range of frictions. Note that we only used the real-time flux autocorrelation function up to $\beta\hbar = 1578$ au. Near the turnover friction, the STACEM method slightly overestimates the transmission coefficient; however, it does capture the turnover from energy to spatial diffusion. Still, by increasing the included PIMC data range to $t = 2\beta\hbar$, we were able to obtain the correct quantum transmission coefficient $\kappa = 3.74$ even at the turnover friction. In the high friction regime, the recrossing is inhibited by the rapid dissipation because of the bath. As a result, the real-time flux autocorrelation function decays on a fast-time scale ensuring that the calculation of the rate using short-time data is accurate. More importantly, the rates estimated by the STACEM method exhibit excellent agreement with the exact quantum results in the weak coupling regime as well, even though significant recrossing is possible under these conditions.

An Arrhenius plot of the rate constant for a very weak friction strength is shown in Figure 4. At the temperatures higher than the crossover temperature (estimated as $T_c \approx 100$ K), we observe a linear behavior characteristic of activated barrier crossing. Conversely, at lower temperatures, tunneling dominates the dynamic process and the rate constant becomes temperature independent. For these low-temperature calculations, MC data with a cutoff time less than $\beta\hbar$ was used for the analytic continuation. For example, for $T = 50$ K, the data up to $t = 1500$ au $\approx 0.25\beta\hbar$ was used to compute the rate. Note that the correct temperature independent tunneling rates are obtained at low temperatures, which additionally confirms the applicability of the analytic continuation method even in the deep tunneling regime.

B. Primary Charge Separation in the Photosynthetic Reaction Center. In contrast to the typical adiabatic reaction studied in the previous section, we consider a nonadiabatic reaction in this section. The primary charge separation of photosynthesis in bacterial reaction centers involves electron transfer from an excited special chlorophyll pair (the donor) to a bacteriopheophytin of the L branch (the acceptor). Despite the large (17 Å, center-to-center) distance between these two sites,[67] the electron transfer is characterized by a time constant of about 3 ps and a quantum yield close to unity. Understanding the specifics of this highly efficient electron-transfer process has been the subject of numerous experimental and theoretical studies. Following the work of Makri and co-workers,[68,69] it is now generally accepted that the mechanism of this primary charge transfer is sequential with a low energy bridge of bacteriochlorophyll monomer located between the donor and the acceptor. A series of experiments with subpicosecond resolution have been performed on the reaction centers of *Rhodopseudomonas viridis* and *Rhodobacter sphaeroides* to determine the kinetic features of the primary charge separation process and its temperature dependence.[70−76] Among many studies involving mutants of the reaction center, Holten and co-workers[77] have studied a double mutant with an aspartic acid introduced near ring V of bacteriochlorophyll monomer in a *Rhodobacter capsulatus* in which bacteriopheophytin is also replaced by bacteriochlorophyll. This double mutant exhibited a slower primary electron transfer to the L-side chromophores with a kinetic constant of 20 ps,[77] which results from the bridge free energy increase from its native value. It was observed that the changes in the energetics induced by the chemical modification of Heller et al.[77] lead to slower kinetics. Sim and Makri[69] estimated the free energy of the reduced accessory bacteriochlorophyll monomer and its coupling to the donor and the acceptor of the double mutant by performing real-time path integral computations of the time evolution of the reduced density matrix. In this study, we adapt the parameters estimated by Sim and Makri[69] and use them to model a discrete two-level system coupled to a harmonic bath model.

The simplest model of nonadiabatic electron transfer is that of a discrete two-state system coupled to a harmonic model of the medium. In this model, the two states, donor and acceptor, are coupled to each other as well as to a harmonic bath that describes collective modes of polarization fluctuations of the medium surrounding the reaction complex, such that the Hamiltonian has the form

$$H = \begin{pmatrix} 0 & -V_{\text{eff}} \\ -V_{\text{eff}} & \Delta G \end{pmatrix} + \sum_{n=1}^{Q} \left\{ \frac{1}{2} M_n \dot{x}_n{}^2 - \frac{1}{2} M_n \omega_n{}^2 \, x_n{}^2 \right\} \begin{pmatrix} 1 & 0 \\ 0 & 1 \end{pmatrix} - \sum_{n=1}^{Q} c_n x_n \begin{pmatrix} -1 & 0 \\ 0 & 1 \end{pmatrix} \tag{47}$$

The flux operator is written as

$$\hat{F} = \frac{i}{\hbar}[\hat{H}_{\text{s}}, \hat{h}_{\text{p}}] \tag{48}$$

where $\hat{H}_{\text{s}}$ corresponds to the system Hamiltonian (2 × 2 matrix in this case) and $\hat{h}_{\text{p}}$ is the product side projection operator. Therefore matrix representation of the flux operator becomes

$$\mathbf{F} = i\frac{V_{\text{eff}}}{\hbar} \begin{pmatrix} 0 & -1 \\ 1 & 0 \end{pmatrix} \tag{49}$$

To model the two-state electron transfer, we assume that in long-distance tunneling the electronic coupling is due to superexchange. The simplest expression for the superexchange coupling is the McConnell product of the form[78,79]

$$V_{\text{eff}} = \frac{V_{12} V_{23}}{E_{\text{b}}} \tag{50}$$

where $V_{12} = 22$ cm^{-1}, $V_{13} = 135$ cm^{-1}, and $E_{\text{b}} = 500$ cm^{-1} resulting in $V_{\text{eff}} = 6$ cm^{-1}. Finally the driving force of the reaction is $\Delta G = -400$ cm^{-1}. The solvent reorganization energy of the system is estimated to be 2000 cm^{-1}, so that, in the case of the wild-type reaction center, the free energy surfaces for the donor and acceptor intersect at the activationless geometry.[68] The reorganization energy λ is defined as the integral of spectral density divided by the frequency

$$\lambda = \frac{4}{\pi} \int_0^\infty \mathrm{d}\omega \, \frac{J(\omega)}{\omega} \tag{51}$$

To satisfy this condition, the friction constant of the ohmic spectral density is set equal to 2.62 and the cutoff frequency is taken to be $\omega_{\text{c}} = 600$ cm^{-1}.

The PIMC simulations performed for this system were slightly different from those described in section III. The path integral expression of the symmetrized flux autocorrelation function eq 3 for a discrete two-level system Hamiltonian is

$$G'_{\text{F}}(t) = \frac{1}{Z_{\text{r}}} \sum_{k_0}^{2} \cdots \sum_{k_{2N+1}}^{2} F_{k_0,k_{2N+1}} F_{k_N,k_{N+1}} \times \prod_{j=N+1}^{2N} \langle u_{k_{j+1}} | \mathrm{e}^{iH_{\text{s}}\Delta t_{\text{c}}^{*}/\hbar} | u_{k_j} \rangle \times \prod_{j=1}^{N} \langle u_{k_j} | \mathrm{e}^{-iH_{\text{s}}\Delta t_{\text{c}}/\hbar} | u_{k_{j-1}} \rangle \, I(\tilde{s}_{k_0},\ldots,\tilde{s}_{k_{2N+1}};\Delta t_{\text{c}}) \tag{52}$$

In this case, we used a random uniform sampling function for MC simulations.

The experimentally measured time constant for this system is 20 ps,[77] whereas the theoretically predicted time constant from the three-state reduced density matrix calculation is 21 ps.[69] Using the STACEM method the time constant obtained from the two-state superexchange model was found to be 28 ps. The same result was obtained using a different spectral density obtained numerically from molecular dynamics simulations by Marchi et al.[80] The reason for this slower kinetics is the assumption of the superexchange electron-transfer mechanism of the two-state model. It has been shown that the bridge state participates in the electron-transfer resulting in a sequential electron-transfer mechanism[68,69] so that the superexchange model of this study using the effective coupling of the superexchange transfer[78,79] was expected to give a slower rate, i.e., a larger time constant.

VI. Concluding Remarks

Motivated by the recent work of Rabani et al.[45] and Krilov et al.[47] we presented the STACEM method for calculating the quantum canonical rate constant from the path integral simulation of short real-time flux autocorrelation functions. The frequency dependent canonical rate constant was expressed as a Fourier transform of the flux autocorrelation function[45] which was calculated for short times by a discretized PIMC sampling technique related to that proposed by Thirumalai and Berne.[53] Taking advantage of accurate short-time quantum correlation functions obtained by the PIMC sampling method, the ME analytic continuation approach was employed to predict long-time behavior of correlation functions. Numerical test cases presented in section V indicate that the STACEM method provides very accurate quantum results for thermally averaged rate constants of nonadiabatic as well as adiabatic chemical reactions under various conditions relevant in chemical reactions, i.e., the crossover and deep tunneling regimes.

In complex condensed phase systems subject to conditions of overdamped friction, quantum coherences dissipate rapidly. Therefore, the description of quantum effects obtained by numerical analytic continuation of short-time dynamical data is expected to be accurate.[47] Thus under the overdamped friction the use of numerical analytic continuation methods for extracting the frequency dependent rate constant from the short-time dynamic data is indeed possible. For the case of underdamped friction, on the other hand, evaluating the exact quantum time correlation function which is stable and free of statistical errors for long times becomes less plausible and it is extremely difficult to determine the plateau time. Nevertheless, the STACEM method seems to provide a practical and reliable way of predicting quantitatively accurate canonical quantum mechanical rate constant provided that the accurate short-time description is available.

It was also found that, despite the bridge free energy being higher than that of the donor state, the nonadiabatic electron transfer in the double mutant of the photosynthetic reaction center still follows (at least partly) the sequential mechanism. Although it has been shown that the bridge state participates in the electron transfer in the wild-type reaction center,[68,69] one cannot rule out the possibility that both superexchange and sequential electron-transfer mechanisms contribute to the electron transfer in the double mutant reaction center which has a high-lying bridge state. The kinetic time constant of the two-state superexchange model was larger than the experimentally measured time constant supporting the argument that the sequential mechanism played a crucial role in the electron transfer when high-lying bridge states are present.

Further applications of the STACEM method are possible for more complicated problems of adiabatic and nonadiabatic reactions in condensed matter,[39] including excitation transfer, energy migration, and superexchange phenomena with multiple barriers.[79,81,82] It likewise would be of interest to study the dependence of the reaction rate on quantum coherence effects, friction, electronic coupling constant between bridges, exothermicity, and temperature. The influence functional approach that appears in this paper is still limited to the harmonic bath with linear coupling. A possible extension allowing for treatment of anharmonic baths is the use of cumulant expansions of the influence functional for the implicit bath modes.[55] In addition, following Rabani et al.,[45] one may treat the bath explicitly thus avoiding the limitation of the harmonic bath assumption in the real-time path integration. In combination with an improved numerical analytic continuation technique and more efficient sampling techniques which provide stable results over long times, it is believed that the study of chemical reactions within a more general environment is possible using the STACEM method presented in this paper. All of these problems will be the subject of future investigation.

Acknowledgment. This paper is dedicated to Bill Miller, a theorist without peer, on the occasion of his 60th birthday. This work was supported by a grant to BJB from the National Science Foundation.

References and Notes

(1) Miller, W. H. *J. Chem. Phys.* **1975**, *62*, 1899.
(2) Miller, W. H. *Faraday Discuss. Chem. Soc.* **1977**, *62*, 40.
(3) Voth, G. A.; Chandler, D.; Miller, W. H. *J. Chem. Phys.* **1989**, *91*, 7749.
(4) Cao, J.; Voth, G. A. *J. Chem. Phys.* **1994**, *100*, 5093, 5096.
(5) Cao, J.; Voth, G. A. *J. Chem. Phys.* **1994**, *101*, 6157, 6168, 6184.
(6) Marcus, R. A.; Coltrin, M. E. *J. Chem. Phys.* **1977**, *67*, 2609.
(7) Truhlar, D. G.; Garrett, B. C. *Annu. Rev. Phys. Chem.* **1984**, *35*, 159.
(8) Truhlar, D. G.; Garrett, B. C. *J. Phys. Chem.* **1992**, *96*, 6515.
(9) Miller, W. H.; Handy, N. C.; Adams, J. E. *J. Chem. Phys.* **1980**, *72*, 90.
(10) Topaler, M.; Makri, N. *J. Chem. Phys.* **1994**, *101*, 7500.
(11) Miller, W. H. *Faraday Discuss.* **1998**, *110*, 1.
(12) Miller, W. H. *J. Phys. Chem. A* **1998**, *102*, 793.
(13) Miller, W. H.; Schwartz, S. D.; Tromp, J. W. *J. Chem. Phys.* **1983**, *79*, 4889.
(14) Yamamoto, T. *J. Chem. Phys.* **1960**, *33*, 281.
(15) Fischer, S. F. *J. Chem. Phys.* **1970**, *53*, 3159.
(16) Chandler, D. *J. Chem. Phys.* **1978**, *68*, 2959.
(17) Wolynes, P. G. *Phys. Rev. Lett.* **1981**, *47*, 968.
(18) Feynman, R. P. *Rev. Mod. Phys.* **1948**, *20*, 367.
(19) Feynman, R. P.; Hibbs, A. *Quantum Mechanics and Path Integrals*; McGraw-Hill: New York, 1965.
(20) Feynman, R. P. *Statistical Mechanics*; Addison-Wesley: Reading, MA, 1998.
(21) Metropolis, N.; Rosenbluth, A. W.; Rosenbluth, M. N.; Teller, A. N.; Teller, E. *J. Chem. Phys.* **1953**, *21*, 1087.
(22) Valleau, J. P.; Whittington, S. G. in *Modern Theoretical Chemistry*; Berne, B. J., Ed.; Plenum: New York, 1977; Vol. 5, p 137.
(23) Berne, B. J.; Thirumalai, D. *Annu. Rev. Phys. Chem.* **1986**, *37*, 401.
(24) Borkovec, M.; Berne, B. J. *J. Chem. Phys.* **1987**, *86*, 2444.
(25) Thirumalai, D.; Bruskin, E. J.; Berne, B. J. *J. Chem. Phys.* **1983**, *79*, 5063.
(26) Cline, R. E., Jr.; Wolynes, P. G. *J. Chem. Phys.* **1988**, *88*, 4334.
(27) Doll, J. D.; Coalson, R. D.; Freeman, D. L. *J. Chem. Phys.* **1987**, *87*, 1641.
(28) Chang, J.; Miller, W. H. *J. Chem. Phys.* **1987**, *87*, 1648.
(29) Filinov, V. S. *Nucl. Phys. B* **1986**, *271*, 717.
(30) Makri, N.; Miller, W. H. *J. Chem. Phys.* **1988**, *89*, 2170.
(31) Mak, C. H.; Chandler, D. *Phys. Rev. A* **1991**, *44*, 2352.
(32) Egger, R.; Mak, C. H. *Phys. Rev. B* **1994**, *50*, 15210.
(33) Makri, N. *Chem. Phys. Lett.* **1992**, *193*, 435.
(34) Makri, N. *J. Chem. Phys.* **1993**, *97*, 2417.
(35) Topaler, M.; Makri, N. *J. Chem. Phys.* **1992**, *97*, 9001.
(36) Makri, N.; Makarov, D. E. *J. Chem. Phys.* **1995**, *102*, 4600, 4611.
(37) Sim, E.; Makri, N. *Chem. Phys. Lett.* **1996**, *249*, 224.
(38) Sim, E.; Makri, N. *Comput. Phys. Commun.* **1997**, *99*, 335.
(39) Topaler, M.; Makri, N. *J. Phys. Chem.* **1996**, *100*, 4430.
(40) Wang, H.; Sun, X.; Miller, W. H. *J. Chem. Phys.* **1998**, *108*, 9726.
(41) Sun, X.; Wang, H. B.; Miller, W. H. *J. Chem. Phys.* **1998**, *109*, 4190.
(42) Sun, X.; Wang, H. B.; Miller, W. H. *J. Chem. Phys.* **1998**, *109*, 7064.
(43) Makri, N.; Thompson, K. *Chem. Phys. Lett.* **1998**, *291*, 101.
(44) Thompson, K.; Makri, N. *J. Chem. Phys.* **1999**, *110*, 1343.
(45) Rabani, E.; Krilov, G.; Berne, B. J. *J. Chem. Phys.* **2000**, *112*, 2605.
(46) Plimak, L.; Pollak, E. *Phys. Rev. E* **2000**, *113*, 4533.
(47) Krilov, G.; Sim, E.; Berne, B. J. *J. Chem. Phys.* **2001**, *114*, 1075.
(48) Harris, D. O.; Engerholm, G. G.; Gwinn, W. D. *J. Chem. Phys.* **1965**, *43*, 1515.
(49) Bacic, Z.; Light, J. C. *Annu. Rev. Phys. Chem.* **1989**, *40*, 469.
(50) Echave, J.; Clary, D. C. *Chem. Phys. Lett.* **1992**, *190*, 225.
(51) Topaler, M.; Makri, N. *Chem. Phys. Lett.* **1993**, *210*, 448.
(52) Berne, B. J.; Harp, G. D. *Adv. in Chem. Phys.* **1970**, *17*, 63.
(53) Thirumalai, D.; Berne, B. J. *J. Chem. Phys.* **1984**, *81*, 2512.
(54) Feynman, R. P.; Vernon, F. L., Jr. *Ann. Phys.* **1963**, *24*, 118.
(55) Makri, N. *J. Phys. Chem. B* **1999**, *103*, 2823.
(56) Skilling, J., Ed.; *Maximum Entropy and Bayesian Methods*; Kluwer: Dordrecht, The Netherlands, 1989.
(57) Gubernatis, J. E.; Jarrell, M.; Silver, R. N.; Silvia, D. S. *Phys. Rev. B* **1991**, *44*, 6011.
(58) Gallicchio, E.; Berne, B. J. *J. Chem. Phys.* **1996**, *105*, 7064.
(59) Gallicchio, E.; Berne, B. J. *J. Chem. Phys.* **1994**, *101*, 9909.
(60) Krilov, G.; Berne, B. J. *J. Chem. Phys.* **1999**, *111*, 9147.
(61) Kim, D.; Doll, J. D.; Gubernatis, J. E. *J. Chem. Phys.* **1997**, *106*, 1641.
(62) Gallicchio, E.; Egorov, S. A.; Berne, B. J. *J. Chem. Phys.* **1998**, *109*, 7745.
(63) Lawson, C. L.; Hanson, R. J. *Solving Least Squares Problems*; Prentice Hall: Upper Saddle River, NJ, 1974.
(64) Miller, K. *SIAM J. Math. Anal.* **1970**, *1*, 52.
(65) Jarrell, M.; Gubernatis, J. E. *Phys. Rep.* **1996**, *269*, 133.
(66) Bryan, R. K. *Eur. Biophys. J.* **1990**, *18*, 165.
(67) Diesenhofer, J.; Epp, O.; Miki, K.; Huber, R.; Michel, H. *J. Mol. Biol.* **1984**, *180*, 385.
(68) Makri, N.; Sim, E.; Topaler, M.; Makarov, D. E. *Proc. Natl. Acad. Sci. U.S.A.* **1996**, *93*, 3926.
(69) Sim, E.; Makri, N. *J. Phys. Chem. B* **1997**, *101*, 5446.

(70) Holten, D.; Hoganson, C.; Windson, M. W.; Schenck, C. C.; Parsons, W. W.; Migus, A.; Fork, R. L.; Shank, C. V. *Biochim. Biophys. Acta* **1980**, *592*, 461.

(71) Woodbury, N. W.; Becker, M.; Middendort, D.; Parson, W. W. *Biochemistry* **1985**, *24*, 7516.

(72) Martin, J. L.; Breton, J.; Hoff, A. J.; Migus, A.; Antonetti, A. *Proc. Natl. Acad. Sci. U.S.A.* **1986**, *83*, 957.

(73) Breton, J.; Martin, J. L.; Migus, A.; Antonetti, A.; Arszag, A. *Proc. Natl. Acad. Sci. U.S.A.* **1986**, *83*, 5121.

(74) Breton, J.; Martin, J. L.; Fleming, G. R.; Lambry, J.-C. *Biochemistry* **1988**, *27*, 9276.

(75) Fleming, G. R.; Martin, J. L.; Breton, J. *Nature (London)* **1988**, *333*, 190.

(76) Chan, C.-K.; DiMagno, T. J.; Chen, L. X.-Q.; Norris, J. R.; Fleming, G. R. *Proc. Natl. Acad. Sci. U.S.A.* **1991**, *88*, 11202.

(77) Heller, B. A.; Holten, D.; Kirmaier, C. *Science* **1995**, *269*, 1995.

(78) McConnell, H. M. *J. Chem. Phys.* **1961**, *35*, 508.

(79) Beratan, D. N.; Betts, J. N.; Onuchic, J. N. *Science* **1991**, *252*, 1285.

(80) Marchi, M.; Gehlen, J. N.; Chandler, D.; Newton, M. *J. Am. Chem. Soc.* **1993**, *115*, 4178.

(81) Scholes, G. D.; Ghiggino, K. P. *J. Chem. Phys.* **1995**, *103*, 8873.

(82) Segal, D.; Nitzan, A.; Davis, W. B.; Wasielewski, M. R.; Ratner, M. A. *J. Phys. Chem. B* **2000**, *104*, 3817.